




Dynamics and rheology of a single two-dimensional multilobe vesicle in a confined geometry

Mehdi Abbasi ^{1,*}, Alexander Farutin,¹ Abdessamad Nait-Ouhra ^{1,2,3}, Hamid Ez-Zahraouy,²
Abdelilah Benyoussef ⁴ and Chaouqi Misbah^{1,†}

¹Univ. Grenoble Alpes, CNRS, LIPhy, F-38000 Grenoble, France

²LaMCSel, Faculty of Sciences, Mohammed V University of Rabat, Rabat 1014 Morocco

³Université de Lorraine, CNRS, GeoRessources, Nancy 54000, France

⁴Hassan II Academy of Science and Technology, Rabat 10220, Morocco



(Received 7 July 2021; accepted 15 August 2022; published 13 September 2022)

A vesicle is a common model used to represent red blood cell (RBC) *in silico* and *in vitro*. We investigate here the dynamics and the rheology of a vesicle under shear flow confined between two parallel walls in wide ranges of applied shear rate and the viscosity contrast (viscosity ratio between the internal and external fluids of the vesicle). The Helfrich model is used to describe the vesicle membrane energy and the spectral boundary integral method to compute the velocity of the vesicle membrane. Multilobe shapes are observed in a wide range of shear rates and viscosity contrasts. A phase diagram is determined in this parameter space. The cytoskeleton of a RBC is not necessary for the multilobe manifestation, in contrast with recent claims. Here we show that these shapes are due to membrane tension only. This highlights the fact that the two-dimensional (2D) vesicle model used here, besides its relevant predictions in previous studies (such as slipper and parachute shapes), can capture several other shapes and dynamics observed for RBCs. The 2D vesicle can thus be used as a reliable model, at least as an exploration basis, to investigate blood flow where the three-dimensional model may prove to be computationally demanding, especially for dense suspensions. We investigate the rheology of the multilobe shapes in the dilute regime and find that the effective viscosity exhibits a significant jump associated with a transition to multilobe dynamics. We provide simple interpretations to these findings. We discuss the stability of the centered solutions and the emergence of the off-centered ones.

DOI: [10.1103/PhysRevFluids.7.093603](https://doi.org/10.1103/PhysRevFluids.7.093603)

I. INTRODUCTION

Blood is a complex fluid, with about 55% of its volume consisting of plasma and 45% is composed of red blood cells (RBCs), whereas white blood cells and platelets together account for less than 1%. The RBCs are responsible for oxygen transport from lungs to the tissues and the removal of the carbon dioxide from the tissues to the lungs. RBCs are not oxygen carriers only, but they also transport several other chemical species, the most prominent of which is ATP, playing a pivotal role in blood flow regulation via a complex biochemical signaling involving endothelial cells [1,2]. The alteration of RBC dynamics and morphologies may influence the blood viscosity and thus blood perfusion, impacting the distribution of oxygen, and other species, to tissues and organs [3]. The dynamics and the morphology of RBCs and of their biomimetic counterparts (vesicles

* mehdi.abbasi@univ-grenoble-alpes.fr

† chaouqi.misbah@univ-grenoble-alpes.fr

and capsules) have been the subject of intensive studies during the last two decades, theoretically [4–7], experimentally [8–16], and numerically [17–25]. In blood circulation, RBCs have the ability to assume several morphologies. The most common shapes are (1) parachute, which is a symmetric shape [26,27], and (2) the asymmetric shape, called a slipper [11,19,27,28], to cite a few examples. More recent studies reported the existence of other shapes (snaking, pin, peanut) [29]. Under shear flow, a single RBC exhibits three main dynamics: (1) tank-treading motion (TT) where the cell adopts a fixed orientation and its membrane rotates like a tank tread [30–32], (2) tumbling (TB) motion where the cell flips like a solid particle [13,31], and (3) vacillating breathing (also called swinging) [6,33], where the cell orients along some direction and its long axis undergoes oscillations.

One of the main questions is to identify whether or not a given shape or dynamics is common to a wide range of soft particles (like vesicles, capsules, RBCs), or if it is specific to a given type of particle. Most of the aforementioned dynamics, under both shear and Poiseuille flows, are common to RBCs, vesicles and capsules [9,13,20,34–40]. Vesicles are two-dimensional (2D) incompressible fluid membranes that form a closed surface containing fluid inside. The membrane is composed of two layers of phospholipid molecules, each having a hydrophilic head and two hydrophobic tails [41]. Vesicles are characterized by a bending rigidity of the membrane and the ratio between the viscosities of the internal and the external fluids. Contrary to vesicles, capsules are endowed with shear elasticity, mimicking the cytoskeleton of RBCs. The bending of the membrane is generally described by the Helfrich model [42], which involves the membrane curvature. The Skalak model [43] is generally used to describe the shear elasticity of the cytoskeleton of RBCs (spectrin network). From a mechanical point of view vesicles differ from RBCs by the absence of shear elasticity due to cytoskeleton. Despite this simplification, vesicles have often revealed to have many shapes and dynamics in common with RBCs. The comparison between vesicles and RBCs can help identifying features which are specific or not to cytoskeleton. For example, at low shear rates the RBC model exhibits TB, whereas vesicles show TT at low enough viscosity contrast for any shear rate. The occurrence of TB for RBCs at low shear rates is due to the cytoskeleton, since TT of RBCs would be accompanied by a distortion of cytoskeleton that is significant in comparison to a TB regime. It is only at high enough shear rate (when hydrodynamic shear stress overcomes elastic stress due to cytoskeleton) that RBCs show TT. Regarding shapes, such as slipper or parachute, they are known to be exhibited both by RBCs and vesicles, and the role of cytoskeleton affects only their occurrence region in the parameter space.

In a more recent study [44], Lanotte *et al.* have reported experimentally on a type of shape exhibited by RBCs at high enough shear rates, which has been named the multilobe shape (see later). This shape was briefly discussed earlier by Fischer [45]. Subsequently, a systematic numerical study [46] was devoted to these morphologies using two different simulation techniques (dissipative particle dynamics and volume of fluid method), taking into account the cytoskeleton shear elasticity, bending rigidity, and cytosol viscosity. A rich phase diagram showing a transition from TB to multilobe (MB) shapes at high viscosity contrast and high shear rate has been reported. It has been concluded that the cytoskeleton elasticity has an essential role in the manifestation of the MB shape.

The purpose of this paper is to contribute to the understanding of the minimal ingredients for the occurrence of the MB shapes and investigate the effect of this shape on the rheology. We have thus conducted 2D simulations for a confined vesicle model (only membrane bending is included). Our results show that MB does exist in this model, ruling thus out the necessity of cytoskeleton. In addition, as these shapes appear at high enough shear rates, bending elasticity is not essential either (they occur in a regime where hydrodynamic shear stress overcome bending stress). Our results clearly show that the birth of MB is due to competition between the applied flow and tension of the membrane. We will present a full phase diagram, in the plane of flow strength and viscosity contrast. The MB shapes appear at high enough shear rates and high enough viscosity contrast, as obtained in three dimensions for the RBC model [46]. We shall see that there are two branches of MB solutions that can coexist in some range of parameters. These two branches correspond to solutions that are regular or irregular in time. Which branch is chosen depends on the initial configuration. The next

step will be dedicated to the study of rheological properties, namely, the effective viscosity and normal stress difference. We find that the MB transition is accompanied by a significant change of the intrinsic viscosity as well as the normal stress difference. We will provide a few qualitative explanations for these behaviors.

II. MODEL

A. Fluid flow

We focus here on the simplest model (2D phospholipid vesicle), where only bending elasticity and membrane incompressibility are included. The 2D vesicle model has been shown to capture several known characteristics for RBCs. Shapes like parachute and slipper [19,47], dynamics such as TB and TT [21,48] are manifested by both systems (RBCs and 2D vesicles). Other phenomena such as lateral migration of RBCs [49] and the shapes of RBCs within aggregates [50–52] have been shown to be captured by the 2D vesicle model.

The 2D vesicle is represented by a membrane contour that contains a viscous fluid inside and is suspended in another fluid filling the channel. The internal fluid viscosity is denoted as η_1 and the suspending fluid viscosity as η_0 . The system is bounded by two rigid walls located at $y = 0$ and $y = L_y$, where L_y is the channel width. The fluid in the channel is subject to a linear shear flow $v_x^\infty(y) = \dot{\gamma}(y - L_y/2)$ where $\dot{\gamma}$ is the shear rate. Periodic boundary conditions are used along x axis (the flow direction). The period L_x is taken large enough in order to avoid any artifact due to periodic boundary conditions. Typically $L_x = 4L_y$ has proven to be sufficient for our purposes.

The RBCs typical linear size is about $3 \mu\text{m}$, and under physiological conditions the typical shear rate value at the vessel wall, which depends on vessel diameter, ranges from 10^2 s^{-1} to 10^4 s^{-1} [53]. The blood plasma viscosity is about $\eta_0 = 10^{-3} \text{ mPa s}$. The Reynolds number, by taking the RBC size as a length scale, is quite small (in the range 10^{-4} to 10^{-2}), so that it is legitimate to take the zero Reynolds number limit. In this case the velocity of the inner (i.e., inside the vesicle) and the outer fluids is described by the Stokes equations:

$$-\nabla P + \eta_i \Delta \mathbf{v} = 0, \quad (1)$$

$$\nabla \cdot \mathbf{v} = 0, \quad (2)$$

where $i = 0$ inside the vesicle and $i = 1$ outside the vesicle, P is the pressure, and \mathbf{v} is the velocity field. The Stokes equations (1) and (2) are supplemented by the following boundary conditions:

- (1) The no-slip boundary conditions at the walls
- (2) The periodic boundary conditions for the velocity \mathbf{v} and the pressure P
- (3) The continuity of the fluid velocity at the membrane
- (4) The force balance at the membrane, which dictates that the sum of the viscous forces applied by the inner and outer fluids on the membrane is balanced by the membrane force \mathbf{f} , the expression for which is given below.

These boundary conditions define a unique solution of Eqs. (1) and (2), which depends on the membrane conformation and forces \mathbf{f} .

B. Membrane forces

The force applied by the membrane on the surrounding fluid is obtained by a functional derivative of the following energy, which is the sum two contributions: the bending energy (the Helfrich energy [54]) and the membrane incompressibility contribution:

$$E = \frac{k_b}{2} \oint_m c^2 ds + \oint_m \zeta ds, \quad (3)$$

where s represents the curvilinear coordinate on the vesicle contour, c is the local curvature of the membrane, k_b is the membrane bending rigidity, and ζ is a local Lagrange multiplier associated with

the constraint of local perimeter inextensibility. The functional derivative (providing the force) of the bending energy can be found in Ref. [55]. The total force has the following form:

$$\mathbf{f} = k_b \left[\frac{d^2 c}{ds^2} + \frac{1}{2} c^3 \right] \mathbf{n} - c \zeta \mathbf{n} + \frac{d\zeta}{ds} \mathbf{t}, \quad (4)$$

\mathbf{n} and \mathbf{t} are the normal and tangential unit vectors, respectively. The force can be rewritten in a dimensionless form:

$$\bar{\mathbf{f}} = \left[\frac{d^2 \bar{c}}{d\bar{s}^2} + \frac{1}{2} \bar{c}^3 \right] \mathbf{n} - \bar{c} \bar{\zeta} \mathbf{n} + \frac{d\bar{\zeta}}{d\bar{s}} \mathbf{t}, \quad (5)$$

where dimensionless variables are defined as follows:

$$\bar{f} = \frac{R_0^3 f}{k_b}, \quad \bar{c} = c R_0, \quad \bar{s} = \frac{s}{R_0}. \quad (6)$$

Here $R_0 = (A_0/\pi)^{1/2}$ is the characteristic size of the vesicle (A_0 is the area inside the vesicle). Due to some computational reasons, we do not use $\bar{\zeta}$ directly in the numerical scheme of the force. The local extension of the membrane is instead prevented by the penalization energy E_{tens} that replaces the second term in the right-hand side of Eq. (3):

$$E_{\text{tens}} = \frac{k_s}{2} \int_0^1 \left(\frac{ds}{d\alpha} - L \right)^2 d\alpha, \quad (7)$$

where k_s is the extension modulus of the membrane, L is the prescribed perimeter of the vesicle, and α is the reference coordinate. The reference coordinate is used to parametrize the position of the membrane points as $\mathbf{r}_{\text{mem}}(\alpha)$. We choose the parametrization in such a way that the position $\mathbf{r}_{\text{mem}}(\alpha)$ travels exactly the whole membrane as α increases continuously from 0 to 1. The parametrization is continued periodically for other values of alpha: $\mathbf{r}_{\text{mem}}(\alpha + 1) = \mathbf{r}_{\text{mem}}(\alpha)$.

The tension force for energy (7) is

$$\mathbf{f}_{\text{tens}} = \frac{d\tilde{\zeta}}{ds} \mathbf{t} - c \tilde{\zeta} \mathbf{n}, \quad \text{where} \quad \tilde{\zeta} = k_s (ds/d\alpha - L), \quad (8)$$

which coincides with the tension contribution in Eq. (4) with the Lagrange multiplier ζ replaced by the local tension $\tilde{\zeta}$. Furthermore, the tension $\tilde{\zeta}$ in Eq. (8) tends to the Lagrange multiplier ζ as k_s is increased to infinity.

Equation (8) provides an explicit link between the stretching of the membrane and the local tension. The cost of this simplification is that the local arc length is never exactly equal to the prescribed value p_0 . However, this difference is negligible for large enough k_s . We set $k_s R_0^3/k_b = 4 \times 10^3$ in our simulations, which results in a good conservation of local arc length for all parameters explored in this study.

C. Dimensionless parameters

Dimensionless numbers are used to describe the vesicle and the flow characteristics:

The capillary number: Allows one to quantify the flow strength over bending rigidity of the membrane

$$C_a = \frac{\eta_0 \dot{\gamma} R_0^3}{k_b} \equiv \dot{\gamma} \tau_c. \quad (9)$$

The confinement: Describes the ratio between the effective diameter of the vesicle and the channel width

$$C_n = \frac{2R_0}{L_y}. \quad (10)$$

The viscosity contrast: The ratio between the viscosities of the internal and external fluids

$$\lambda = \frac{\eta_1}{\eta_0}. \quad (11)$$

The reduced area: Combining the vesicle perimeter L and its enclosed area A_0 :

$$\tau = \frac{(A_0/\pi)}{(L/2\pi)^2}. \quad (12)$$

Throughout this paper, we will use the following scales: R_0 for the distance, τ_c for the time, and η_0 for the viscosity.

III. NUMERICAL PROCEDURE

A. General outline

In order to preserve high accuracy we use Fourier basis for discretization of all functions on the membrane contour and compute all derivatives in Fourier domain [56,57]. The shape of the vesicle at time t is described by a periodic function $\mathbf{r}_{\text{mem}}(\alpha, t)$ of the reference coordinate α , as defined above. We parametrize this function by a Fourier series

$$r_{\text{mem},x}(\alpha) + ir_{\text{mem},y}(\alpha) = \sum_{k=-k_{\text{max}}}^{k_{\text{max}}} r_k e^{2\pi i k \alpha}, \quad (13)$$

where the complex amplitudes r_k are the shape parameters of the membrane and k_{max} defines the number of Fourier harmonics used to represent the membrane shape (typically, we use $k_{\text{max}} = 31$, which gives 63 harmonics in total).

One time step of the simulation takes a set of values of r_k and proceeds as follows:

- (1) We use r_k to reconstruct the shape of the membrane $\mathbf{r}_{\text{mem}}(\alpha, t)$, and the derivatives $\partial_\alpha \mathbf{r}_{\text{mem}}(\alpha, t)$, $\partial_{\alpha\alpha} \mathbf{r}_{\text{mem}}(\alpha, t)$.
- (2) We use $\mathbf{r}_{\text{mem}}(\alpha, t)$, $\partial_\alpha \mathbf{r}_{\text{mem}}(\alpha, t)$, and $\partial_{\alpha\alpha} \mathbf{r}_{\text{mem}}(\alpha, t)$ to compute the membrane force, membrane normal, arc length element of the membrane, perimeter, enclosed area, and so on.
- (3) We use the above force, shape, normal, and arc element to compute the flow in the channel.
- (4) We expand the velocity field at the membrane into a Fourier series and update the Fourier components r_k .

The implementation details for steps 2 and 3 are given below. Step 4 is done using a simple explicit Euler scheme. This step also involves a procedure to conserve exactly the area enclosed by the membrane contour. Physically, this area is conserved by the incompressibility of the enclosed fluid and the impermeability of the membrane but this exact conservation is lost after numerical discretization. We thus use homogeneous deflation or inflation along the normal direction to conserve the area inside the vesicle at each time step.

B. Force calculation

We compute the force directly in the Fourier space by taking the variation of the membrane energies (3) and (7) with respect to the amplitudes r_k . The energy itself is calculated in the coordinate space, by discretizing the membrane contour by a large number of points homogeneously distributed in the α space $\alpha_i = i/N_{\text{mem}}$, $i \in \{0, 1, \dots, N_{\text{mem}} - 1\}$. Here N_{mem} is the number of points used to discretize the membrane; we take $N_{\text{mem}} \geq 2(k_{\text{max}} + 1)$.

The derivatives with respect to the arc length are calculated as $\partial_s = \partial_\alpha / (ds/d\alpha)$. The integration with respect to the arc length element is reduced to the integration with respect to α by the substitution $ds = d\alpha (ds/d\alpha)$. Here $ds/d\alpha = |d\mathbf{r}_{\text{mem}}/d\alpha|$. The integration with respect to α is performed using the trapezoid rule (here the sum over all α_i divided by N_{mem}). This method shows super-algebraic convergence with N_{mem} for smooth periodic functions. The Fourier components of

the membrane force are calculated from the virtual work principle, using the variation $E \rightarrow E + \delta E$ of the energy upon a small variation of the membrane shape $\mathbf{r}_{\text{mem}}(\alpha) \rightarrow \mathbf{r}_{\text{mem}}(\alpha) + \delta \mathbf{r}_{\text{mem}}(\alpha)$:

$$\begin{aligned} \delta E &= - \oint \mathbf{f} \cdot \delta \mathbf{r}_{\text{mem}} ds = -\text{Re} \int_0^1 \left(\sum_{k=-k_{\text{max}}}^{k_{\text{max}}} F_k e^{2\pi k i \alpha} \right)^* \left(\sum_{k'=-k_{\text{max}}}^{k_{\text{max}}} \delta r_k e^{2\pi k' i \alpha} \right) d\alpha \\ &= - \sum_{k=-k_{\text{max}}}^{k_{\text{max}}} \text{Re}(F_k^* \delta r_k), \end{aligned} \quad (14)$$

where F_k and δr_k are the coefficients of the Fourier series for $[f_x(\alpha) + i f_y(\alpha)] ds/d\alpha$ and $\delta r_{\text{mem},x}(\alpha) + i \delta r_{\text{mem},y}(\alpha)$, respectively. We thus define the force amplitudes from Eq. (14) as

$$\text{Re } F_k = - \frac{\partial E}{\partial \text{Re } r_k}, \quad \text{Im } F_k = - \frac{\partial E}{\partial \text{Im } r_k}. \quad (15)$$

Calculating the amplitudes F_k allows us to reconstruct the forces $\mathbf{f} ds/d\alpha$ which are used to calculate the fluid velocity as explained below.

C. Flow solver

Due to the linearity of Stokes equations we can transform the set of fluid equations into an integral equation which is nonlocal. This is based on the use of Green's function techniques [58]. This method enjoys quite a good precision. We used the Green's functions that satisfy directly the no-slip boundary condition at the channel walls in our previous works. Those Green's functions do not have an explicit representation in elementary functions. Instead, the Green's function values were calculated numerically on a fixed grid and stored in a table. The values for arbitrary positions were obtained by interpolation. Here we use a different approach which we have found to result in lower computational cost of the simulation, in particular for a dense suspension. We take the Green's functions that satisfy the periodic boundary conditions along the x direction and use an explicit discretization of the wall. The wall force and residual velocity at the wall are parametrized by a Fourier series thanks to the periodicity in x direction, as explained below. The advantage of this method is that a relatively small number of Fourier harmonics is sufficient to reduce the residual velocity at the wall to machine precision, unless there are membrane points very close to the wall. This is because the self-interactions of the walls are calculated exactly in Fourier space using analytical expressions.

The velocity at any point \mathbf{r} in the simulation domain satisfies the following equation:

$$\Lambda(\mathbf{r}) \mathbf{v}(\mathbf{r}) = \mathbf{v}^\infty(\mathbf{r}) + \mathbf{v}^{\text{ves}}(\mathbf{r}) + \mathbf{v}^{\text{wall}}(\mathbf{r}), \quad (16)$$

where $\mathbf{v}^\infty(\mathbf{r})$ is the imposed velocity field (a linear shear flow as defined above), \mathbf{v}^{ves} is the velocity field produced by the vesicles, and \mathbf{v}^{wall} is the velocity field produced by the wall. The coefficient Λ is defined as

$$\Lambda(\mathbf{r}) = \begin{cases} \lambda & \text{if } \mathbf{r} \text{ is inside a vesicle} \\ (1 + \lambda)/2 & \text{if } \mathbf{r} \text{ is on a vesicle membrane} \\ 1 & \text{if } \mathbf{r} \text{ is outside all vesicles or is on a wall.} \end{cases} \quad (17)$$

Here λ is the viscosity contrast defined as $\lambda = \frac{\eta_1}{\eta_0}$. The vesicle contribution is defined as

$$\mathbf{v}^{\text{ves}}(\mathbf{r}) = \frac{1}{\eta_0} \oint_m \underline{\underline{G}}(\mathbf{r}_0, \mathbf{r}) \cdot \mathbf{f}(\mathbf{r}_0) ds(\mathbf{r}_0) + (1 - \lambda) \oint_m \underline{\underline{v}}(\mathbf{r}_0) \cdot \underline{\underline{T}}(\mathbf{r}_0, \mathbf{r}) \cdot \mathbf{n}(\mathbf{r}_0) ds(\mathbf{r}_0), \quad (18)$$

where $\underline{\underline{G}}(\mathbf{r}_0, \mathbf{r})$ and $\underline{\underline{T}}$ are the Green's functions (G_{ij} refers to the so-called single-layer contribution, while T_{ijk} accounts for the double-layer contribution). Here we take the Green's functions satisfying periodic boundary conditions in x direction, which have a known expression in terms of elementary

TABLE I. Simulation parameters.

Parameters	Simulation unit	Physical unit
k_b	0.1	4×10^{-19} J
R_0	1.0	$3 \mu\text{m}$
η_0	1.0	1 mPa s
τ_c	10.0	0.54 s

functions [58]. These functions reduce the integration over an infinite array of image vesicles arranged periodically in the x direction to an integral over a single vesicle inside the computational domain. The integration in Eq. (18) is thus taken along the membranes of all vesicles in the computational domain.

Note that the above Green's functions do not satisfy the no-slip boundary condition at the walls (in contrast to one of our previous studies [59]), therefore the contribution of the walls to the velocity field has to be taken explicitly. This contribution should precisely guarantee the no-slip condition at the walls. The wall contribution is written as

$$\mathbf{v}^{\text{wall}}(\mathbf{r}) = \frac{1}{\eta_0} \oint_{\text{walls}} \underline{\underline{G}}(\mathbf{r}_w, \mathbf{r}) \cdot \mathbf{f}^w(\mathbf{r}_w) dx, \quad (19)$$

where \mathbf{r}_w is wall position and $\mathbf{f}^w(\mathbf{r}_w)$ is the density of forces applied by the wall on the fluid at a position \mathbf{r}_w . The wall force is not known *a priori* and needs to be solved for to satisfy the no-slip condition at the wall, as described below. The contour integral along the walls is simplified to the integral with respect to the x coordinate in Eq. (19). Note that the above contribution is similar in form to the first contribution in (18), because in applying the Green's theorem one has to integrate over all boundaries (vesicle and bounding walls).

The no-slip boundary conditions at the walls are implemented in the following way: Because the velocity of the walls is defined by the imposed shear flow $[\mathbf{v}^\infty$ in Eq. ((16), the no-slip condition reduces to

$$\mathbf{v}^{\text{ves}}(\mathbf{r}^w) + \mathbf{v}^{\text{wall}}(\mathbf{r}^w) = 0 \quad (20)$$

for all \mathbf{r}^w at the wall. The first term in Eq. (20) is given explicitly by Eq. (18), while the second term is related by a linear operator to the wall forces. We thus need to solve Eq. (20) for the wall forces. The next step is to use the obtained wall forces to calculate the flow \mathbf{v}^{wall} on the vesicle membranes, using Eq. (19). The wall forces and the velocity fields measured at the wall remain invariant after translation by L_x in x direction due to the periodic boundary conditions. We thus represent these three fields by Fourier series in x :

$$\begin{aligned} v_x^{\text{ves}}(x, L_y/2 \pm L_y/2) + i v_y^{\text{ves}}(x, L_y/2 \pm L_y/2) &= \sum_{k=(1-N_w)/2}^{(N_w-1)/2} v_{k,u/l}^{\text{ves}} e^{2\pi i k x / L_x}, \\ v_x^{\text{wall}}(x, L_y/2 \pm L_y/2) + i v_y^{\text{wall}}(x, L_y/2 \pm L_y/2) &= \sum_{k=(1-N_w)/2}^{(N_w-1)/2} v_{k,u/l}^{\text{wall}} e^{2\pi i k x / L_x}, \\ f_x^{\text{wall}}(x, L_y/2 \pm L_y/2) + i f_y^{\text{wall}}(x, L_y/2 \pm L_y/2) &= \sum_{k=(1-N_w)/2}^{(N_w-1)/2} f_{k,u/l}^{\text{wall}} e^{2\pi i k x / L_x}, \end{aligned} \quad (21)$$

where $v_{k,u/l}^{\text{ves}}$, $v_{k,u/l}^{\text{wall}}$, and $f_{k,u/l}^{\text{wall}}$ are the corresponding Fourier components. The second index u in $v_{k,u/l}^{\text{ves}}$ refers to the upper wall [$y = L_y$ in the left-hand side of Eq. (21)], while l refers to the lower wall [$y = 0$ in the left-hand side of Eq. (21)]. N_w sets the number of Fourier harmonics used for wall discretization.

The coefficients $v_{k,u/l}^{\text{ves}}$ can be calculated directly without calculating the velocity at the wall in the coordinate space:

$$v_{k,u/l}^{\text{ves}} = \frac{1}{\eta_0} \oint_m \mathbf{G}_{k,u/l}(\mathbf{r}_0) \cdot \mathbf{f}(\mathbf{r}_0) ds(\mathbf{r}_0) + (1 - \lambda) \oint_m \mathbf{v}(\mathbf{r}_0) \cdot \underline{\underline{T}}_{k,u/l}(\mathbf{r}_0) \cdot \mathbf{n}(\mathbf{r}_0) ds(\mathbf{r}_0), \quad (22)$$

where the kernels $\mathbf{G}_{k,u/l}(\mathbf{r}_0)$ and $\underline{\underline{T}}_{k,u/l}(\mathbf{r}_0)$ depend only on the wall position and L_x . These kernels can be expressed in elementary functions as shown in Ref. [58].

The amplitudes $v_{\pm k,u/l}^{\text{wall}}$ and $f_{\pm k,u/l}^{\text{wall}}$ can be related to each other as

$$(v_{\pm k,u/l}^{\text{wall}}) = \frac{1}{\eta_0} G^{\text{wall}}(k)(f_{\pm k,u/l}^{\text{wall}}), \quad (23)$$

where $(v_{\pm k,u/l}^{\text{wall}})$ and $(f_{\pm k,u/l}^{\text{wall}})$ are 4D complex vectors composed of the corresponding components and $G^{\text{wall}}(k)$ is a 4×4 complex matrix, which depends only on L_x and L_y and whose explicit expression is given in Ref. [58].

The wall force amplitudes are thus obtained by solving

$$(v_{k,u/l}^{\text{ves}}) + \frac{1}{\eta_0} G^{\text{wall}}(k)(f_{\pm k,u/l}^{\text{wall}}) = 0, \quad k \geq 0 \quad (24)$$

for the four-dimensional complex vector $(v_{k,u/l}^{\text{ves}})$ computed from Eq. (22). Note that Eq. (24) is degenerate for $k = 0$, since normal forces with constant amplitude produce no flow.

Finally, the wall contribution to the velocity field in the fluid domain can be obtained from known $(f_{\pm k,u/l}^{\text{wall}})$ as

$$\mathbf{v}^{\text{wall}}(\mathbf{r}) = \frac{1}{\eta_0} \sum_{j \in \{u,l\}} \sum_{k=(1-N_w)/2}^{(N_w-1)/2} G_{k,j}(\mathbf{r}) f_{k,j}^{\text{wall}}. \quad (25)$$

IV. RESULTS

A. The effect of the confinement on the phase diagram

We have fixed the reduced area to 0.65 which is the typical value for RBCs, and we have analyzed systematically the vesicle dynamics at low confinement ($C_n = 0.2$), where the walls play a minor role. The simulations parameters used throughout this article are tabulated in Table I. The vesicle center was located on the central axis of the channel. The stability of such centered solutions is discussed below.

We have produced a phase diagram [Fig. 1(a)] in a wide range of capillary number C_a and viscosity contrast λ . Many previous studies [48,60–63] have investigated the dynamics of a single vesicle under shear flow using 2D simulations, but we are not aware of a previous report on a multilobe vesicle. Despite quite high values of shear rates the perimeter and the surface of the vesicle are well conserved during the simulation; the relative error of the perimeter is less than 1% in all our simulations. Three regimes have been identified: tank treading (TT), tumbling (TB), and multilobe (MB). The present phase diagram is in a good qualitative agreement with Ref. [46] (their Fig. 2). In other words, the topologies of both phase diagrams are quite similar, in the sense that the relative positions of the three modes in the phase diagram present the same typical picture: at low viscosity contrast λ TT always prevails as shown in Ref. [48]. In our phase diagram TT remains stable at high capillary number showing no transition, whereas at high viscosity contrast λ , the TB prevails at small shear rate $\dot{\gamma}$ and undergoes a transition towards MB at high shear rate $\dot{\gamma}$. Note that the rolling stomatocyte, discocyte, and tumbling stomatocytes in three dimensions [46] all degenerate into TB in two dimensions, since there is no other analog in two dimensions. Figure 1(a) shows three transitions, from TB to MB occurring at $\lambda \geq 5.8$ and in the range of $35 \leq C_a \leq 50$, the second transition takes place from TT to MB occurring at $\lambda \geq 5.7$ and $C_a \geq 38$, and the last transition is between TT and TB at $C_a < 35$ and $5.5 \leq \lambda \leq 5.8$.

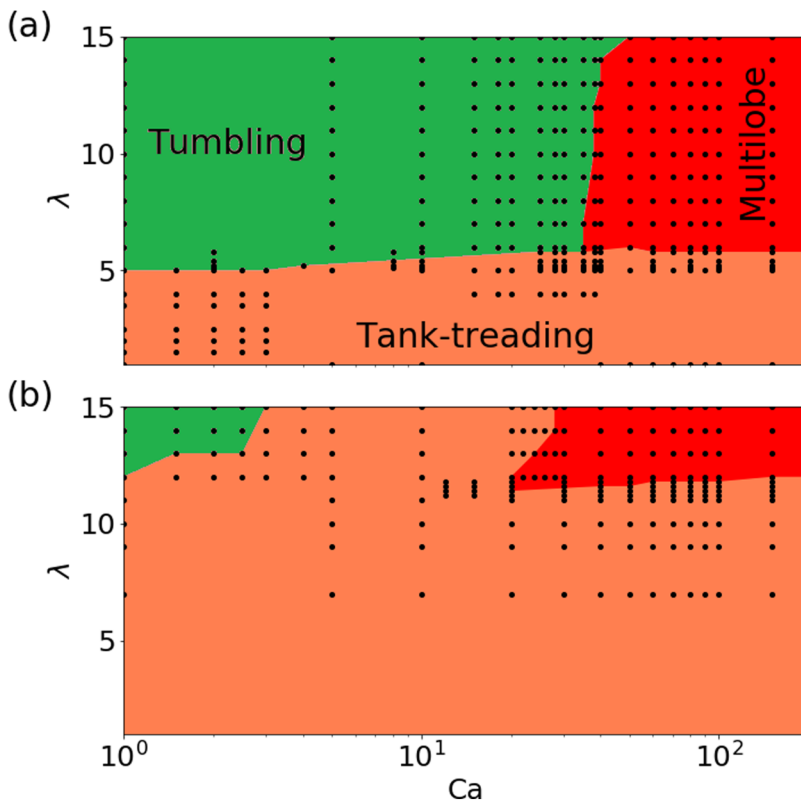


FIG. 1. Phase diagrams showing the dynamics of a single vesicle. The simulation data are shown as dots. (a) $C_n = 0.2$, (b) $C_n = 0.4$. Top and bottom have the same color code.

We have investigated the effect of confinement on the evolution of the phase diagram. By reducing the distance between the two walls ($C_n = 0.4$) we have observed that the confinement plays an essential role regarding the MB shape [Fig. 1(b)]. Indeed the area of MB phase shrinks by about twice when the confinement is doubled, and TT prevails in this case. It is likely that walls affect excursion of membrane protrusions (which are pronounced for MB) and tend to reduce the domain of existence of MB phase.

Figure 2 shows snapshots of the MB mode (see the corresponding movie in the Supplemental Material [64]). Two types of MB motions can be identified: the irregular one [Fig. 2(a)] and the regular one [Figs. 2(b) and 2(c)]. We have found that these two motion types correspond to different branches of MB solutions that can coexist in a certain region of λ : We have analyzed this coexistence by tracing the bending energy of the vesicle as a function of λ for $C_n = 0.2$ and $C_a = 100$ using two initial configurations, one corresponding to the irregular MB solution [such as the one shown in Fig. 2(a)] and the other one corresponding to the regular MB solution [such as the one shown in Fig. 2(c)]. The final state of the two MB solutions at a nearby value of λ was used as the initial states of the simulation in order to follow both branches as far as possible. The results are shown in Fig. 3. As can be seen, three different branches of multilobe dynamics can be identified: a chaotic motion with irregular protrusions traveling along the membrane and two types of trilobe dynamics. Interestingly, the transitions between the states are discontinuous.

If the initial configuration is prepared to be an elliptical vesicle in the channel center as shown in Fig. 4, in the multilobe regime the vesicle starts tumbling and after a few τ_c it undergoes a transition towards a quadrilobe shape which is unstable (transient state) and persists for less than $1000\tau_c$. Over long time the shape becomes a trilobe (a stable shape). Note that, in agreement with our finding, the

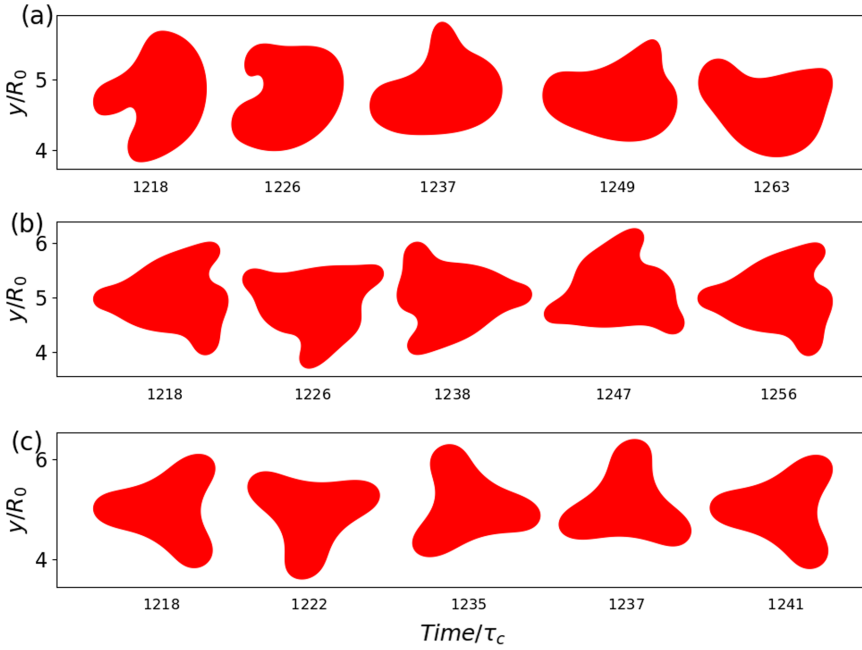


FIG. 2. Snapshots showing dynamics of a single vesicle. We set $C_n = 0.2$ and $C_a = 60.0$. (a) $\lambda = 5.8$, (b) $\lambda = 7.0$, (c) $\lambda = 14.0$. Snapshots (a) show the evolution of the vesicle shape (see movie 1 [64]). Panels (b) and (c) show the dynamics of a vesicle over one period (see movie 1 [64]).

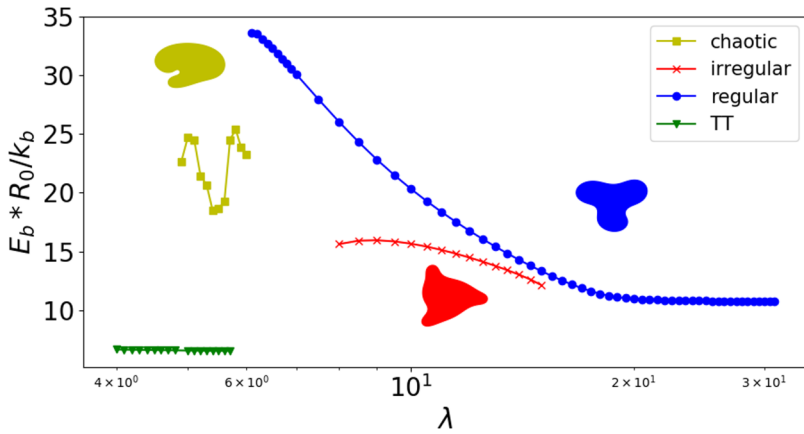


FIG. 3. Average bending energy of vesicle shapes as a function of viscosity contrast. Insets show characteristic shape sequences for different types of multilobe dynamics. $C_n = 0.2$, $C_a = 100$.

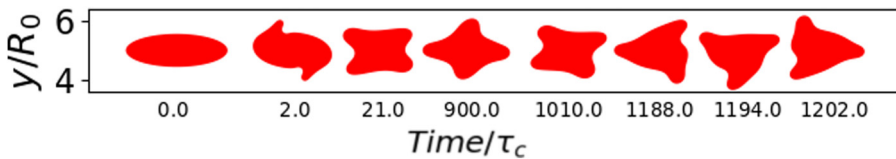


FIG. 4. Snapshots show the evolution of the vesicle shape from the initial configuration to the steady state. Here we set the confinement $C_n = 0.2$, the capillary number $C_a = 60.0$, and the viscosity contrast $\lambda = 7.0$ (see movie 2 [64]). The steady-state dynamic is shown in movie 1 [64].

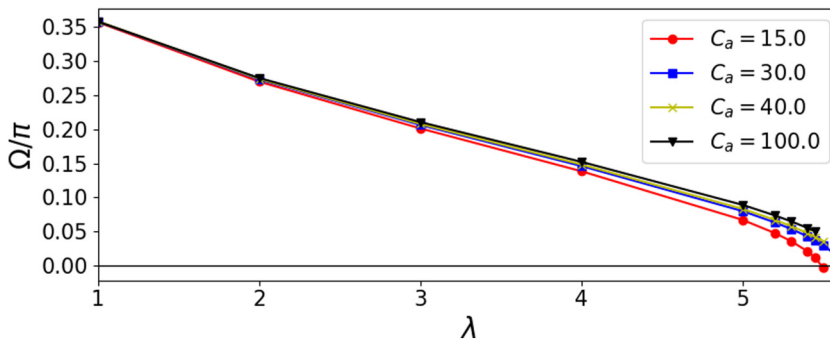


FIG. 5. Vesicle orientation angle as a function of viscosity contrast λ .

quadrilobe shape is not observed as a permanent state in the three-dimensional (3D) simulations of Refs. [44,46].

We clearly see that the MB shape occurrence does not require a shear elasticity of the cytoskeleton. The MB shapes occur at large enough capillary numbers where also the bending rigidity is not essential (large capillary number, where MB occurs, means that bending stress is small in comparison to imposed hydrodynamic stress). These shapes result solely from an interplay between tension (resisting compression) and the imposed flow. This finding corroborates the fact that most of the shapes and dynamics observed so far for RBCs are also common to pure lipid vesicles. Typical examples are parachute shape, slipper, bullets, croissant, and so on, exhibited by vesicles and RBCs both experimentally and numerically.

Finally, it is interesting to note that the topology of phase diagram [Fig. 1(a)] is very reminiscent of that studied in three dimensions for vesicles by several groups [20,65–69], where the relative position of TT, TB and MB phases (obtained here) are to be compared to those corresponding to TT, TB, and VB (vacillating breathing, aka swinging, trembling, initially reported in Ref. [6]). It is tempting to speculate that the mechanism behind the manifestation of MB mode is similar to that of VB mode. Initially the VB phase was studied for a quasispherical vesicle, in which the amplitude of membrane deformation in the VB phase is small. Later, a numerical study dealing with more deflated vesicles [23] shows shapes similar, to some extent, to the MB ones (see Figs. 2 and 3 in Ref. [23]). Like the VB mode [6] the MB mode takes place from TT mode when the angle of orientation of the vesicle with respect to the flow direction is close to zero (positive or negative small values of the angle). Figure 5 shows the behavior of this angle as a function of viscosity contrast λ . This type of behavior is also reported for 3D simulations of RBCs [46]; the MB shape takes place when the orientation angle is close to zero.

B. The rheology of multilobe vesicles

The aim of this section is to investigate the effect of the MB shape discussed above on the rheological behavior of a single vesicle. We quantify the normalized viscosity and the normalized normal stress difference. The effective viscosity has the following form:

$$\eta = \eta_0(1 + [\eta]\phi), \quad (26)$$

where ϕ is the suspension concentration, equal to the ratio between the vesicle area and the area of the calculation domain, and $[\eta]$ is the normalized viscosity (called also the intrinsic viscosity when $\phi \rightarrow 0$) representing the vesicle contribution to the viscosity. The effective viscosity is the ratio between the xy component of stress tensor and the applied shear rate:

$$\eta = \frac{\langle \sigma_{xy} \rangle}{\dot{\gamma}}, \quad (27)$$

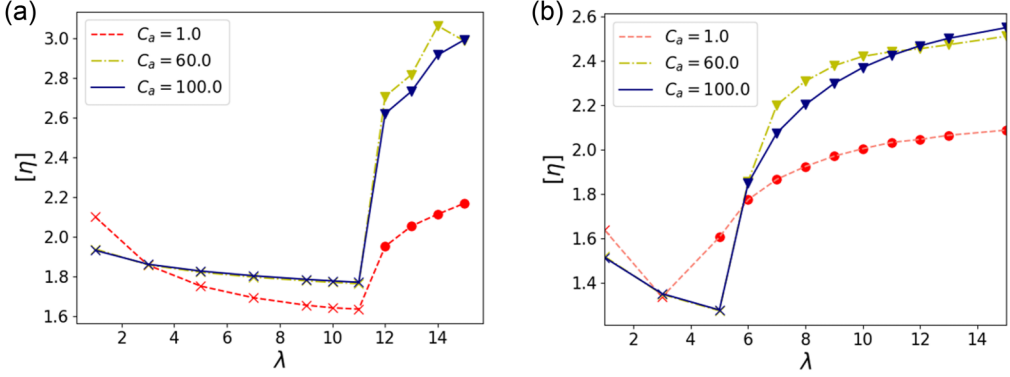


FIG. 6. The normalized effective viscosity $[\eta]$ as a function of viscosity contrast λ for different capillary number C_a . Circle symbols correspond to tumbling, crosses to tank treading, and triangles to multilobes. Left: $C_n = 0.4$; right: $C_n = 0.2$.

where the bracket $\langle \cdot \rangle$ denotes an average over the wall length. Alternatively the viscosity can also be obtained as an integral over the vesicle perimeter. Following the Batchelor formula [70], the normalized effective viscosity is given by

$$[\eta] = \frac{\eta - \eta_0}{\eta_0 \phi} = \frac{1}{\eta_0 A_0 \dot{\gamma}} \left[- \int_m y f_x ds + \eta_0 (\lambda - 1) \int_m (n_x v_y + n_y v_x) ds \right]. \quad (28)$$

The first term of the normalized viscosity describes the dynamical contribution which is due to the membrane force, and the second term is the kinematic contribution of the vesicle (the membrane velocity). The normal stress difference is defined as $N = \langle \sigma_{xx} \rangle - \langle \sigma_{yy} \rangle$, which was normalized as

$$[N] = \frac{\langle \sigma_{xx} \rangle - \langle \sigma_{yy} \rangle}{(\eta - \eta_0) \dot{\gamma}} \quad (29)$$

in Ref. [71]. Here the averaged stress tensor is given by

$$\begin{aligned} \langle \sigma_{ij} \rangle &= \frac{1}{L_x L_y} \int_{\text{box}} [-P \delta_{ij} + \eta_0 (\partial_i v_j + \partial_j v_i)] dA - \frac{1}{L_x L_y} \int_m r_j f_i ds \\ &+ \eta_0 \frac{(1 - \lambda)}{L_x L_y} \int_m (n_i v_j + n_j v_i) ds, \end{aligned} \quad (30)$$

where δ_{ij} is the Kronecker symbol, and r_i is a component (x or y) of the membrane position vector. The first integral is performed over the calculation domain. Here, the vesicle dynamic plays a crucial role on the rheology. The pertinent parameters of interest are the viscosity contrast and the capillary number. It has been reported in Refs. [72,73] that the effective viscosity of a single vesicle is not monotonous with the viscosity contrast λ , the minimum of the effective viscosity is associated with the critical value of the viscosity contrast of the transition between tank treading and tumbling. The effective viscosity was found to decrease with the viscosity contrast in the TT regime and suddenly increases after the transition to the TB regime. Figure 6 shows the behavior of the effective viscosity as a function of viscosity contrast λ . We see there the above feature, namely, that the viscosity decreases with λ in the TT regime and increases in the TB one. Here we find that the viscosity increases in the MB regime, as with the TB one, but here the increase is relatively more pronounced. Despite the fact that the area spanned by a TB vesicle is larger than with a MB vesicle, the resulting effect on viscosity due to a MB vesicle is larger. We believe that the presence of

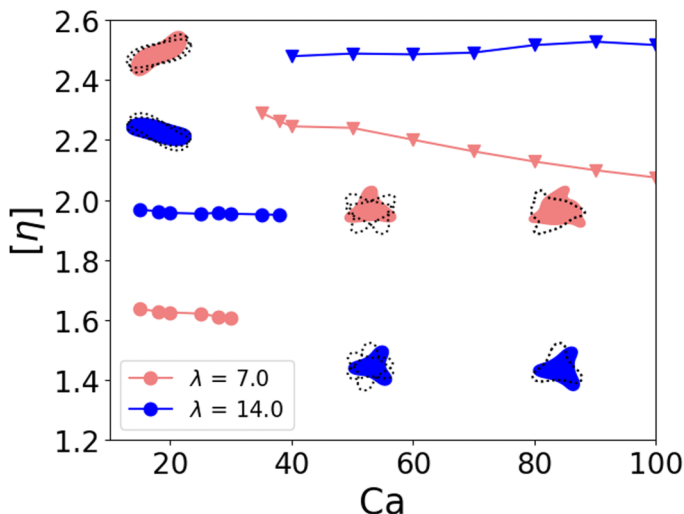


FIG. 7. The normalized viscosity $[\eta]$ as a function of capillary number Ca for different viscosity contrast λ . The confinement is $C_a = 0.2$. Circles correspond to the TB and triangles to MB dynamics.

protuberance in the MB shape cause a stronger dissipation in the surrounding fluid, resulting in a higher dissipation. During tumbling of MB the presence of three protuberances causes a higher average (over a period which corresponds to a membrane material point making a full turn) cross section against flow as compared to a TB vesicle.

Let us analyze the evolution of viscosity as a function of capillary number. It has been reported that the effective viscosity of a vesicle suspension may exhibit both shear thinning and shear thickening depending on the viscosity contrast [74]. For a given viscosity contrast and upon increasing capillary number, we have a transition from TB to MB (Fig. 1). In the TB regime we find a weak shear thinning (Fig. 7). At the TB-MB transition the viscosity exhibits a large jump. In this sense the system exhibits a sudden shear thickening. Within the MB regime, and for not too large viscosity contrast, the suspension shows a shear thinning. For a large enough viscosity contrast the suspension viscosity exhibits a plateau. The sudden increase of the viscosity in the MB regime is traced back to a higher cross section (as explained above). The increase of viscosity in the MB regime is consistent with the experimental report shown in Fig. 4 of Ref. [44]. The shear thinning in the MB regime (red triangles in Fig. 7) is due to the fact that the MB shape explores less space as the capillary number increases. To quantify this effect, we plot the center of mass as a function of time for two capillary numbers (Fig. 8). For each case the center of mass describes an ellipse with

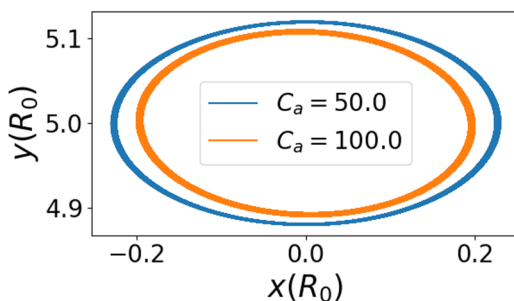


FIG. 8. The center of mass trajectory for two capillary numbers.

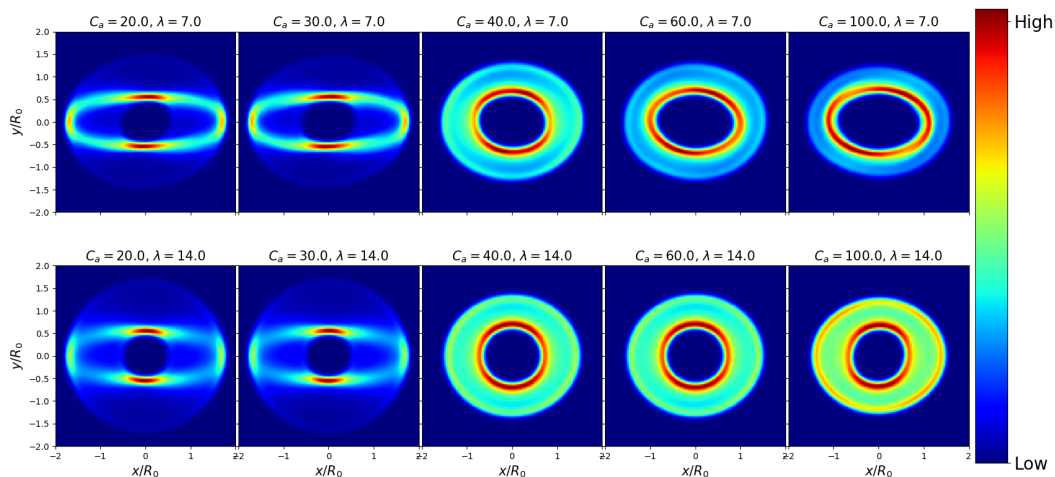


FIG. 9. The average occupancy as a function of C_a for two different values of λ .

an area which decreases with C_a , causing a smaller viscosity. We have further analyzed the origin of the behavior of the viscosity. We determine the average (over long time) of the occupancy of the cell in the channel. This is reported in Fig. 9 as a function of C_a for different values of viscosity contrast λ . We find the following features: (1) when we cross the boundary (as a function of C_a) of the TB-MB phase (occurring at about $C_a \sim 40$) the average occupancy jumps meaning the cell explores more the channel width, and this triggers a jump in the viscosity. (2) For the upper panel, in the MB occupancy decreases with C_a , explaining the shear thinning for $\lambda = 7$. (3) In the lower panel the occupancy in the MB phase remains practically constant leading to a plateau in the viscosity behavior.

The interpretation of the normalized normal stress difference is more complicated than the normalized effective viscosity. In the TB regime the normal stress difference (Fig. 10) is almost zero, before becoming negative (meaning contractile stress) and then acquires a large enough positive value in the MB regime. The membrane incompressibility is a main ingredient, but it enters in an indirect way. The sign of the normal stress difference in the TT regime is fixed by the angle between the flow direction and the long axis of the vesicle (see analytical study in Ref. [72]). In the TB regime there is periodic evolution of normal stress difference during time (the modulus of the maximum

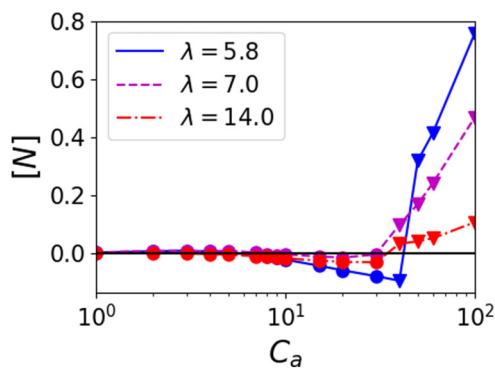


FIG. 10. The normalized normal stress difference $[N]$ as a function of capillary number C_a for different viscosity contrast λ . $C_a = 0.2$. Circles correspond to TB and triangles to MB dynamics.

and the minimum are equal), and because it switches from positive to negative and it vanishes when averaged over a period. In the MB regime the vesicle undergoes a complex dynamics. In the vicinity of the TB-MB transition N is negative (contractile), before becoming positive. Sufficiently far from the transition point the vesicle with a lower viscosity contrast has the highest value of normal stress difference. This is traced back to the flexible nature of the shape deformation for low enough viscosity contrast. In Ref. [72] it has been shown that normal stress difference depends quadratically with shape amplitude deformation. This gives a hint that less viscous vesicles provide a higher stress due to their larger flexibility. It would be interesting to perform systematically a perturbative theory, as in Refs. [6,65–67], in order to analyze analytically the behaviors reported here.

C. Relation between normal stress difference and migration

It is known that the sign of normal stress difference is related to the lateral migration of particles in a suspension [75]. Here we use this relation and the measurements of N , obtained above, to analyze the stability of the centered position of the vesicle. Let us first write the relation between N and migration velocity in a channel which will inform us on the direction of migration as a function of the sign of the normal stress difference. For a semiconfined geometry, in which the migration is caused by a single wall (or in a channel so wide that the effect of the farther wall can be neglected), the migration velocity v_m can be calculated analytically and reads

$$v_m = \frac{NL_x L_y}{8\pi\eta_0(y_0 - y_{\text{wall}})}, \quad (31)$$

where y_0 is the lateral position of the vesicle center and y_{wall} is the wall position. Equation (31) is an asymptotic expression, valid for $|y_0 - y_{\text{wall}}| \gg R_0$. This equation is valid whether the wall is above ($y_0 - y_{\text{wall}} < 0$) or below ($y_0 - y_{\text{wall}} > 0$) the vesicle. For more details and explanations for Eq. (31) see Ref. [76].

For a vesicle close to the channel center the contributions of both walls have to be taken into account. The sum of the expressions (31) with y_{wall} equal to the upper and lower wall positions gives the migration velocity that is only qualitatively correct. This sum however gives the correct scaling for the migration velocity close to the channel center:

$$v_m = -\chi \frac{N(y_0 - L_y/2)L_x}{\eta_0 L_y}, \quad (32)$$

where χ is a numerical constant independent of the channel geometry (as discussed in supplemental material of Ref. [77]). The asymptotic expression (32) is valid under assumptions $|y - L_y/2| \ll R_0 \ll L_y$. We find $\chi = 0.488$ by analyzing the flow due to a point stresslet in an infinite channel.

Figure 11 shows the comparison between the migration velocity predicted by Eq. (32) and the numerical simulation: We place a vesicle close to a wall and measure the lateral migration velocity v_m as a function of the lateral position y . We then compare the rescaled velocity $v_m L_y / \dot{\gamma} R_0^2$ with the theoretical prediction $-\chi N(y - L_y/2)L_x / (\dot{\gamma} \eta_0 R_0^2)$. As can be seen, the agreement is only qualitative for $L_y = 10R_0$ because of the effect of higher-order multipoles in the flow perturbation produced by the vesicle. Increasing L_y to $20R_0$ gives a much better agreement because the effect of higher-order multipoles neglected in (32) diminishes with increasing channel width. Further increasing L_y to $40R_0$ makes the numerical curve almost coincide with the analytical expression close to the channel center. We also observe that changing vesicle parameters, such as viscosity contrast, or reduced area (not shown) does not affect the validity of (32).

Expressions (31) and (32) show that both the particle's migration close to a wall and the stability its centered position are intimately linked to the sign of the normal stress difference generated by the particle.

According to formula (32), the migration is directed towards center of the channel when $N > 0$ and away from center in the opposite case. We have investigated the migration for $N > 0$ and $N < 0$

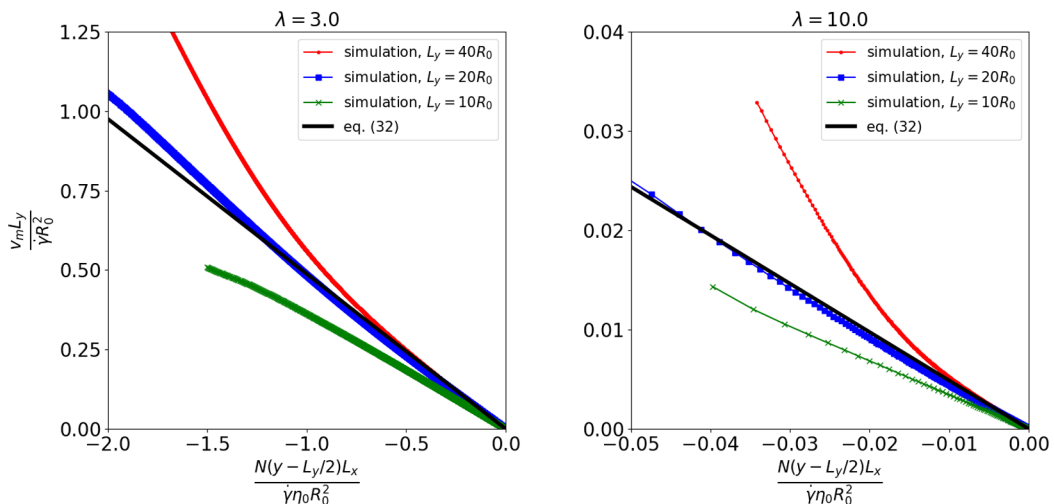


FIG. 11. Rescaled migration velocity as a function of rescaled lateral position, measured numerically and predicted with Eq. (32). Left: $\lambda = 3.0$ the vesicle shows tank treading, and right $\lambda = 10.0$ the vesicle shows multilobe.

by considering a vesicle which is initially localized at different initial positions. When $N > 0$ we have found that an initial position away from center always leads to an inward migration that pushes the vesicle towards the center. The steady final position (which is defined by the y position reaching a fixed position in time, also by perturbing the final position we could ascertain the stability of the final position) is at the center (Fig. 12) (red circles; the channel width is $L_y = 10R_0$ and center of the channel is at $y/R_0 = 5$). When $N < 0$ the migration is found to be outwards, and the vesicle settles at an off-centered position (red crosses in Fig. 12). It is seen that the value of C_a at which there is a transition from an off-centered to a centered position occurs is approximately equal to that corresponding to the passage of N from positive to negative (see Fig. 10). The blue symbols in Fig. 12 refer to situations where the final position depends on initial position. These position values correspond to a coexistence zone between a centered and off-centered position. The bifurcation structure in Fig. 12 reveals a subcritical nature. Thus we see that the migration and the normal stress difference are intimately related.

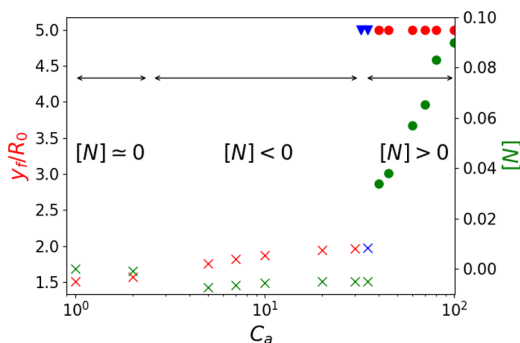


FIG. 12. Final vesicle position y_f/R_0 for different values of C_a . $L_y = 10R_0$; the center of the channel is at $y_f/R_0 = 5$. $\lambda = 14$. The red circles correspond to final position with $N > 0$, the red crosses to $N < 0$. The blue symbols represent positions which depend on initial conditions. The green symbols represent the normal stress difference.

V. SUMMARY AND CONCLUDING REMARKS

A main outcome here is the fact that the cytoskeleton of a RBC is not essential for the MB shape manifestation; only membrane tension is responsible for this effect, since the MB phase takes place at high enough capillary number, meaning that shear stress overcomes bending resistance. It is already known that many shapes known for 2D and 3D vesicles (slipper, croissant, parachute, etc.) [71,78–83] are shared by RBCs models. The present finding provides further evidence highlighting that a 2D vesicle model already captures many important features. The 2D model can be (due to its rapid handling from computational point of view) very useful in exploring new phenomena, especially for dense suspensions, before resorting to the computationally more expensive RBC model. An interesting line of future investigation is the analytical study of MB shapes, following the methods exposed in Refs. [6,65–67]. In those studies either second spherical harmonic [6,65,66] (this is the first excited mode in a linear shear flow), or the fourth-order harmonic [67] have been included; including the fourth-order harmonic turned out to be decisive to account for full numerical simulations. In that study centrosymmetry was imposed, an assumption which is clearly not valid for a MB shape. It will be essential to relax this assumption if we wish to account for this new phase. It is hoped to investigate this matter in the future.

ACKNOWLEDGMENTS

We acknowledge financial support from CNES (Centre National d’Etudes Spatiales), as well as having access to experimental data, and the French-German University Programme “Living Fluids” (Grant No. CFDA-Q1-14). The simulations were performed on the Cactus cluster of the CIMENT infrastructure, which is supported by the Rhône-Alpes region (Grant No. CPER07_13 CIRA).

APPENDIX A: DETAILS OF THE NUMERICAL SIMULATION METHOD

1. Green’s functions for periodic boundary conditions

The periodic boundary conditions respect the translational invariance of the Green’s kernels, which depend only on the relative positions of the source and target points, as in the free-space case: $\underline{\underline{G}}(\mathbf{r}_0, \mathbf{r}) = \underline{\underline{G}}(\mathbf{r}_0 - \mathbf{r})$, $\underline{\underline{T}}(\mathbf{r}_0, \mathbf{r}) = \underline{\underline{T}}(\mathbf{r}_0 - \mathbf{r})$. The explicit expressions and their presentation are copied from Ref. [58]. We have made a small correction, as explained below.

Following Ref. [58] we assume the periodicity direction of the system to be oriented along the x axis and the period of the system is given by L_x . This defines the wave number $q = 2\pi/L_x$. Following Ref. [58] we introduce a function A , defined as

$$A(\mathbf{r}) = \frac{1}{2} \ln[\cosh(qr_y) - \cos(qr_x)] - \frac{1}{2} \ln 2. \quad (\text{A1})$$

The function A represents a solution of the Poisson’s equation for a periodic array of point charges. Using this function, the Green’s kernels for the Stokes equation can be written as [58]

$$\underline{\underline{G}}(\mathbf{r}) = \frac{1}{4\pi} \begin{pmatrix} 1 - A - r_y \partial_{r_y} A & r_y \partial_{r_x} A \\ r_y \partial_{r_x} A & -A + r_y \partial_{r_y} A \end{pmatrix}, \quad (\text{A2})$$

$$T_{xx}(\mathbf{r}) = \frac{1}{2\pi} \nabla \cdot [-A, -r_y \partial_{r_x} A],$$

$$T_{xy}(\mathbf{r}) = T_{yx}(\mathbf{r}) = T_{yx}(\mathbf{r}) = \frac{1}{2\pi} \nabla \cdot [r_y \partial_{r_x} A, -A],$$

$$T_{yy}(\mathbf{r}) = T_{xy}(\mathbf{r}) = T_{yx}(\mathbf{r}) = \frac{1}{2\pi} \nabla \cdot [-A, r_y \partial_{r_x} A],$$

$$T_{yy}(\mathbf{r}) = \frac{1}{2\pi} \nabla \cdot [-r_y \partial_{r_x} A, -A]. \quad (\text{A3})$$

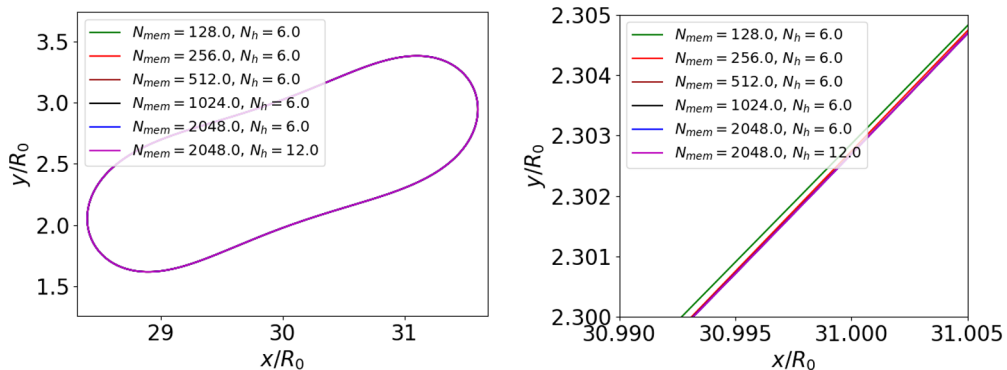


FIG. 13. The configuration of the shape while showing a tank treading. Here we set $C_n = 0.2$, $C_a = 1.0$, and $\lambda = 1.0$. N_h is the number of harmonics. Left fipanel is a zoom of the right one.

Note that we have changed the T_{xxx} expression compared to Ref. [58] (written as $\nabla \cdot [-A, -r_y \partial_{r_x} A]$ there). We have verified that $\nabla \cdot [-A, -r_y \partial_{r_x} A]$ is the correct expression by taking the limit of small q , in which the free-space kernel is recovered, as $T_{xxx}(\mathbf{r}) = -r_x^3/(\pi r^4) + O(q^2)$.

2. Discretization of Eq. (18)

Numerical integration of Eq. (18) requires particular care due to the singular nature of the kernels $\underline{\underline{G}}$ and $\underline{\underline{T}}$, which diverge when the distance between \mathbf{r} and \mathbf{r}_0 tends to 0. We overcome this challenge by a combination of several techniques:

(1) The kernel $\underline{\underline{G}}$ is regularized for $\mathbf{r} = \mathbf{r}_0$ by singularity subtraction technique, in which we subtract an exact identity from the integral in Eq. (18) to make the first integral in Eq. (18) go to zero at $\mathbf{r} = \mathbf{r}_0$ [39].

(2) While the kernel $\underline{\underline{T}}$ diverges at $\mathbf{r}_0 = \mathbf{r}$, the product $\underline{\underline{T}}(\mathbf{r}_0, \mathbf{r}) \cdot \mathbf{n}(\mathbf{r}_0)$ has a finite limit when \mathbf{r}_0 approaches \mathbf{r} along the particle contour. It is thus sufficient to replace the undefined value of the second integral of Eq. (18) for $\mathbf{r}_0 = \mathbf{r}$ with this limit to regularize the second integral [84].

(3) We further improve the precision of computing the integrals in Eq. (18) by using refined meshes to compute the contributions of near-singular points, for which the distance $|\mathbf{r}_0 - \mathbf{r}|$ is comparable to the spacing between the discretization points for the original coarse mesh. This technique is based on decomposing the Green's kernels into a sum of their smoothly varying long-range part and several short-range parts with finite support [85]. The long-range part is then integrated using the most coarse mesh, while the short-range parts are integrated using more refined meshes, where the mesh refinement is consistent with the characteristic length scale of the given short-range contribution to the Green's kernel, which is defined by its support. This method provides a good balance between the computational cost, since the number of kernel evaluations is of the same order for each mesh, and the precision of the method, since the discretization errors due to the singular behavior of the kernels are also of the same order for each mesh.

APPENDIX B: MEMBRANE DISCRETIZATION QUALITY AND BENCHMARKING

The vesicle is described at time t by a closed curve $\mathbf{r}(\alpha, t)$ in (x, y) plane. The membrane is discretized into N_{mem} points. To study the effect of the membrane discretization on the shape of the vesicle, we examine the effect of the variation of the N_{mem} on the vesicle shape as shown in Fig. 13. We see clearly (Fig. 13) that all the vesicle configurations are very close. We set $N_{\text{mem}} = 1024$ in all the simulations presented in this article.

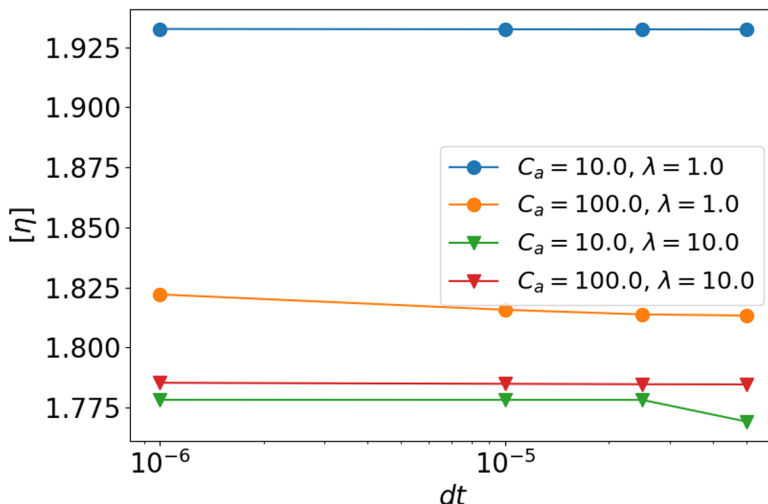


FIG. 14. The normalized effective viscosity as function of the time step for different values of capillary number C_a and viscosity contrast λ . We set $\tau = 0.65$ and $C_n = 0.2$.

We also investigated the effect of the time step dt on the simulation precision. To do this, We calculated the normalized effective viscosity as described in Eq. (29) for different values of capillary number C_a and the viscosity contrast λ . We see clearly (Fig. 14) that the time step value $dt = 10^{-5}$ is the typical value which is independent on the capillary number C_a and the viscosity contrast λ . For calculation speed and accuracy purposes, the time step value is fixed to $dt = 10^{-5}$ in all our simulations in this article.

Finally, we present here a qualitative and quantitative comparison of our simulations with other method. The selected method is lattice Boltzmann method (LBM). For comparison purposes and code validation we show (Fig. 15) the steady inclination angle of the vesicle as function of the confinement C_n , our simulation result is in a good qualitative and quantitative agreement with LBM [60].

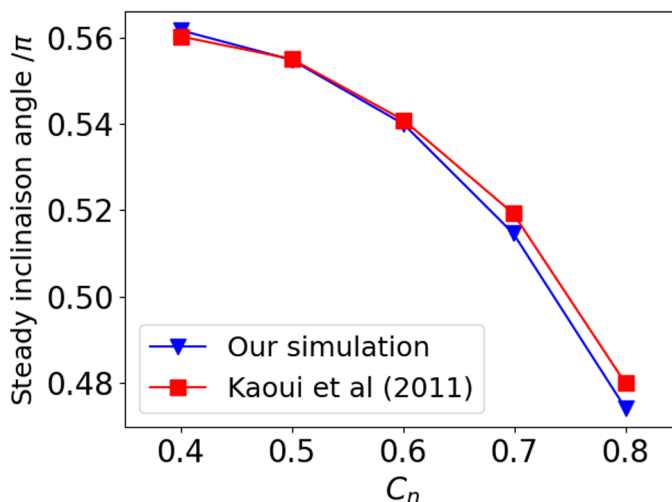


FIG. 15. The variation of the steady inclination angle associated to a vesicle performing tank-treading motion in confined geometries as function of the confinement C_n . We set $\tau = 0.9$ and $C_a = 1.0$ and $\lambda = 1.0$. The data were extracted from Kaoui *et al.* [60].

- [1] E. M. Schwiebert and A. Zsembery, Extracellular ATP as a signaling molecule for epithelial cells, *Biochim. Biophys. Acta (BBA): Biomembranes* **1615**, 7 (2003).
- [2] H. Zhang, Z. Shen, B. Hogan, A. I. Barakat, and C. Misbah, ATP release by red blood cells under flow: Model and simulations, *Biophys. J.* **115**, 2218 (2018).
- [3] R. M. Bateman, M. D. Sharpe, and C. G. Ellis, Bench-to-bedside review: Microvascular dysfunction in sepsis—Hemodynamics, oxygen transport, and nitric oxide, *Critical Care* **7**, 359 (2003).
- [4] S. R. Keller and R. Skalak, Motion of a tank-treading ellipsoidal particle in a shear flow, *J. Fluid Mech.* **120**, 27 (1982).
- [5] U. Seifert, Fluid membranes in hydrodynamic flow fields: Formalism and an application to fluctuating quasispherical vesicles in shear flow, *Eur. Phys. J. B* **8**, 405 (1999).
- [6] C. Misbah, Vacillating Breathing and Tumbling of Vesicles under Shear Flow, *Phys. Rev. Lett.* **96**, 028104 (2006).
- [7] S. Kessler, R. Finken, and U. Seifert, Elastic capsules in shear flow: Analytical solutions for constant and time-dependent shear rates, *Eur. Phys. J. E* **29**, 399 (2009).
- [8] T. M. Fischer, M. Stohr-Lissen, and H. Schmid-Schonbein, The red cell as a fluid droplet: Tank tread-like motion of the human erythrocyte membrane in shear flow, *Science* **202**, 894 (1978).
- [9] M. Abkarian, M. Faivre, and A. Viallat, Swinging of Red Blood Cells under Shear Flow, *Phys. Rev. Lett.* **98**, 188302 (2007).
- [10] V. Kantsler, E. Segre, and V. Steinberg, Dynamics of interacting vesicles and rheology of vesicle suspension in shear flow, *Europhys. Lett.* **82**, 58005 (2008).
- [11] G. Tomaiuolo, M. Simeone, V. Martinelli, B. Rotoli, and S. Guido, Red blood cell deformation in microconfined flow, *Soft Matter* **5**, 3736 (2009).
- [12] G. Couplier, A. Farutin, C. Minetti, T. Podgorski, and C. Misbah, Shape Diagram of Vesicles in Poiseuille Flow, *Phys. Rev. Lett.* **108**, 178106 (2012).
- [13] J. Dupire, M. Socol, and A. Viallat, Full dynamics of a red blood cell in shear flow, *Proc. Natl. Acad. Sci. USA* **109**, 20808 (2012).
- [14] M. Abkarian, M. Faivre, R. Horton, K. Smistrup, C. A. Best-Popescu, and H. A. Stone, Cellular-scale hydrodynamics, *Biomed. Mater.* **3**, 034011 (2008).
- [15] T. M. Fischer and R. Korzeniewski, Threshold shear stress for the transition between tumbling and tank-treading of red blood cells in shear flow: Dependence on the viscosity of the suspending medium, *J. Fluid Mech.* **736**, 351 (2013).
- [16] C. Minetti, V. Audemar, T. Podgorski, and G. Couplier, Dynamics of a large population of red blood cells under shear flow, *J. Fluid Mech.* **864**, 408 (2019).
- [17] C. Quéguiner and D. Barthès-Biesel, Axisymmetric motion of capsules through cylindrical channels, *J. Fluid Mech.* **348**, 349 (1997).
- [18] C. Pozrikidis, Numerical simulation of cell motion in tube flow, *Ann. Biomed. Eng.* **33**, 165 (2005).
- [19] B. Kaoui, G. Biros, and C. Misbah, Why Do Red Blood Cells Have Asymmetric Shapes Even in a Symmetric Flow? *Phys. Rev. Lett.* **103**, 188101 (2009).
- [20] T. Biben, A. Farutin, and C. Misbah, Three-dimensional vesicles under shear flow: Numerical study of dynamics and phase diagram, *Phys. Rev. E* **83**, 031921 (2011).
- [21] H. Zhao and E. S. G. Shaqfeh, The dynamics of a vesicle in simple shear flow, *J. Fluid Mech.* **674**, 578 (2011).
- [22] D. A. Fedosov, M. Peltomäki, and G. Gompper, Deformation and dynamics of red blood cells in flow through cylindrical microchannels, *Soft Matter* **10**, 4258 (2014).
- [23] A. Farutin and C. Misbah, Squaring, parity breaking, and S tumbling of vesicles under shear flow, *Phys. Rev. Lett.* **109**, 248106 (2012).
- [24] R. Trozzo, G. Boedec, M. Leonetti, and M. Jaeger, Axisymmetric boundary element method for vesicles in a capillary, *J. Comput. Phys.* **289**, 62 (2015).
- [25] D. Agarwal and G. Biros, Stable shapes of three-dimensional vesicles in unconfined and confined Poiseuille flow, *Phys. Rev. Fluids* **5**, 013603 (2020).
- [26] R. Skalak and P. I. Branemark, Deformation of red blood cells in capillaries, *Science* **164**, 717 (1969).

- [27] C.-K. Chen and T.-M. Liu, Imaging morphodynamics of human blood cells *in vivo* with video-rate third harmonic generation microscopy, *Biomed. Opt. Express* **3**, 2860 (2012).
- [28] A. Kihm, L. Kaestner, C. Wagner, and S. Quint, Classification of red blood cell shapes in flow using outlier tolerant machine learning, *PLoS Comput. Biol.* **14**, e1006278 (2018).
- [29] O. Aouane, M. Thiébaud, A. Benyoussef, C. Wagner, and C. Misbah, Vesicle dynamics in a confined Poiseuille flow: From steady state to chaos, *Phys. Rev. E* **90**, 033011 (2014).
- [30] H. Schmid-Schönbein and R. Wells, Fluid drop-like transition of erythrocytes under shear, *Science* **165**, 288 (1969).
- [31] H. L. Goldsmith, J. Marlow, and F. C. MacIntosh, Flow behaviour of erythrocytes—I. Rotation and deformation in dilute suspensions, *Proc. R. Soc. London B* **182**, 351 (1972).
- [32] R. Tran-Son-Tay, S. P. Suter, and P. R. Rao, Determination of red blood cell membrane viscosity from rheoscopic observations of tank-treading motion, *Biophys. J.* **46**, 65 (1984).
- [33] H. Noguchi and G. Gompper, Swinging and Tumbling of Fluid Vesicles in Shear Flow, *Phys. Rev. Lett.* **98**, 128103 (2007).
- [34] J. Deschamps, V. Kantsler, and V. Steinberg, Phase Diagram of Single Vesicle Dynamical States in Shear Flow, *Phys. Rev. Lett.* **102**, 118105 (2009).
- [35] X. Shi, S. Wang, and S. Zhang, Numerical simulation of the transient shape of the red blood cell in microcapillary flow, *J. Fluids Struct.* **36**, 174 (2013).
- [36] B. Kaoui, T. Krüger, and J. Harting, How does confinement affect the dynamics of viscous vesicles and red blood cells? *Soft Matter* **8**, 9246 (2012).
- [37] S. Quint, A. F. Christ, A. Guckenberger, S. Himbert, L. Kaestner, S. Gekle, and C. Wagner, 3D tomography of cells in micro-channels, *Appl. Phys. Lett.* **111**, 103701 (2017).
- [38] A. Guckenberger, A. Kihm, T. John, C. Wagner, and S. Gekle, Numerical–experimental observation of shape bistability of red blood cells flowing in a microchannel, *Soft Matter* **14**, 2032 (2018).
- [39] A. Farutin, T. Biben, and C. Misbah, 3D numerical simulations of vesicle and inextensible capsule dynamics, *J. Comput. Phys.* **275**, 539 (2014).
- [40] D. Cordasco, A. Yazdani, and P. Bagchi, Comparison of erythrocyte dynamics in shear flow under different stress-free configurations, *Phys. Fluids* **26**, 041902 (2014).
- [41] R. Lipowsky and E. Sackmann, *Structure and Dynamics of Membranes From Cells to Vesicles*, Handbook 6 of Biological Physics, Vol. 1 (Elsevier, Amsterdam, 1995).
- [42] W. Helfrich, Elastic properties of lipid bilayers: Theory and possible experiments, *Z. Naturforsch. C* **28**, 693 (1973).
- [43] R. Skalak, A. Tozeren, R. P. Zarda, and S. Chien, Strain energy function of red blood cell membranes, *Biophys. J.* **13**, 245 (1973).
- [44] L. Lanotte, J. Mauer, S. Mendez, D. A. Fedosov, J.-M. Fromental, V. Claveria, F. Nicoud, G. Gompper, and M. Abkarian, Red cells’ dynamic morphologies govern blood shear thinning under microcirculatory flow conditions, *Proc. Natl. Acad. Sci. USA* **113**, 13289 (2016).
- [45] T. Fischer and H. Schmid-Schönbein, Tank tread motion of red cell membranes in viscometric flow: Behavior of intracellular and extracellular markers (with film), in *Red Cell Rheology* (Springer, 1978), pp. 347–361.
- [46] J. Mauer, S. Mendez, L. Lanotte, F. Nicoud, M. Abkarian, G. Gompper, and D. A. Fedosov, Flow-Induced Transitions of Red Blood Cell Shapes under Shear, *Phys. Rev. Lett.* **121**, 118103 (2018).
- [47] N. Tahiri, T. Biben, H. Ez-Zahraouy, A. Benyoussef, and C. Misbah, On the problem of slipper shapes of red blood cells in the microvasculature, *Microvasc. Res.* **85**, 40 (2013).
- [48] B. Kaoui, A. Farutin, and C. Misbah, Vesicles under simple shear flow: Elucidating the role of relevant control parameters, *Phys. Rev. E* **80**, 061905 (2009).
- [49] A. Nait-Ouhra, A. Guckenberger, A. Farutin, Hamid Ez-Zahraouy, A. Benyoussef, S. Gekle, and C. Misbah, Lateral vesicle migration in a bounded shear flow: Viscosity contrast leads to off-centered solutions, *Phys. Rev. Fluids* **3**, 123601 (2018).
- [50] D. Flormann, O. Aouane, L. Kaestner, C. Ruloff, C. Misbah, T. Podgorski, and C. Wagner, The buckling instability of aggregating red blood cells, *Sci. Rep.* **7**, 7928 (2017).

- [51] M. Brust, O. Aouane, M. Thiébaud, D. Flormann, C. Verdier, L. Kaestner, M. W. Laschke, H. Selmi, A. Benyoussef, T. Podgorski *et al.*, The plasma protein fibrinogen stabilizes clusters of red blood cells in microcapillary flows, *Sci. Rep.* **4**, 4348 (2014).
- [52] V. Clavería, O. Aouane, Marine Thiébaud, M. Abkarian, G. Coupier, C. Misbah, T. John, and C. Wagner, Clusters of red blood cells in microcapillary flow: Hydrodynamic versus macromolecule induced interaction, *Soft Matter* **12**, 8235 (2016).
- [53] P. Vennemann, R. Lindken, and J. Westerweel, *In vivo* whole-field blood velocity measurement techniques, *Exp. Fluids* **42**, 495 (2007).
- [54] O.-Y. Zhong-can and W. Helfrich, Bending energy of vesicle membranes: General expressions for the first, second, and third variation of the shape energy and applications to spheres and cylinders, *Phys. Rev. A* **39**, 5280 (1989).
- [55] B. Kaoui, G. H. Ristow, I. Cantat, C. Misbah, and W. Zimmermann, Lateral migration of a two-dimensional vesicle in unbounded Poiseuille flow, *Phys. Rev. E* **77**, 021903 (2008).
- [56] S. K. Veerapaneni, D. Gueyffier, D. Zorin, and G. Biros, A boundary integral method for simulating the dynamics of inextensible vesicles suspended in a viscous fluid in 2D, *J. Comput. Phys.* **228**, 2334 (2009).
- [57] S. Dalal, A. Farutin, and C. Misbah, Amoeboid swimming in a compliant channel, *Soft Matter* **16**, 1599 (2020).
- [58] C. Pozrikidis, *Boundary Integral and Singularity Methods for Linearized Viscous Flow* (Cambridge University Press, Cambridge, 1992).
- [59] M. Thiébaud and C. Misbah, Rheology of a vesicle suspension with finite concentration: A numerical study, *Phys. Rev. E* **88**, 062707 (2013).
- [60] B. Kaoui, J. Harting, and C. Misbah, Two-dimensional vesicle dynamics under shear flow: Effect of confinement, *Phys. Rev. E* **83**, 066319 (2011).
- [61] J. Beaucourt, F. Rioual, T. Séon, T. Biben, and C. Misbah, Steady to unsteady dynamics of a vesicle in a flow, *Phys. Rev. E* **69**, 011906 (2004).
- [62] B. Kaoui and J. Harting, Two-dimensional lattice Boltzmann simulations of vesicles with viscosity contrast, *Rheol. Acta* **55**, 465 (2016).
- [63] Y. Kim and M.-C. Lai, Numerical study of viscosity and inertial effects on tank-treading and tumbling motions of vesicles under shear flow, *Phys. Rev. E* **86**, 066321 (2012).
- [64] See Supplemental Material at <http://link.aps.org/supplemental/10.1103/PhysRevFluids.7.093603> for Movie 1 and movie 2 show the shape evolution of the vesicle during time.
- [65] V. V. Lebedev, K. S. Turitsyn, and S. S. Vergeles, Dynamics of Nearly Spherical Vesicles in an External Flow, *Phys. Rev. Lett.* **99**, 218101 (2007).
- [66] G. Danker, T. Biben, T. Podgorski, C. Verdier, and C. Misbah, Dynamics and rheology of a dilute suspension of vesicles: Higher-order theory, *Phys. Rev. E* **76**, 041905 (2007).
- [67] A. Farutin, T. Biben, and C. Misbah, Analytical progress in the theory of vesicles under linear flow, *Phys. Rev. E* **81**, 061904 (2010).
- [68] H. Zhao and E. S. G. Shaqfeh, The dynamics of a non-dilute vesicle suspension in a simple shear flow, *J. Fluid Mech.* **725**, 709 (2013).
- [69] J. Deschamps, V. Kantsler, E. Segre, and V. Steinberg, Dynamics of a vesicle in general flow, *Proc. Natl. Acad. Sci. USA* **106**, 11444 (2009).
- [70] G. K. Batchelor, The stress system in a suspension of force-free particles, *J. Fluid Mech.* **41**, 545 (1970).
- [71] M. Thiébaud, Z. Shen, J. Harting, and C. Misbah, Prediction of Anomalous Blood Viscosity in Confined Shear Flow, *Phys. Rev. Lett.* **112**, 238304 (2014).
- [72] G. Danker and C. Misbah, Rheology of a Dilute Suspension of Vesicles, *Phys. Rev. Lett.* **98**, 088104 (2007).
- [73] G. Ghigliotti, T. Biben, and C. Misbah, Rheology of a dilute two-dimensional suspension of vesicles, *J. Fluid Mech.* **653**, 489 (2010).
- [74] A. N. Ouhra, A. Farutin, O. Aouane, H. Ez-Zahraouy, A. Benyoussef, and C. Misbah, Shear thinning and shear thickening of a confined suspension of vesicles, *Phys. Rev. E* **97**, 012404 (2018).
- [75] J. R. Smart and D. T. Leighton Jr., Measurement of the drift of a droplet due to the presence of a plane, *Phys. Fluids A: Fluid Dyn.* **3**, 21 (1991).

- [76] D. G. Crowdy and Y. Or, Two-dimensional point singularity model of a low-Reynolds-number swimmer near a wall, *Phys. Rev. E* **81**, 036313 (2010).
- [77] H. Wu, M. Thiébaud, W.-F. Hu, A. Farutin, S. Rafai, M.-C. Lai, P. Peyla, and C. Misbah, Amoeboid motion in confined geometry, *Phys. Rev. E* **92**, 050701(R) (2015).
- [78] T. Franke, R. H. W. Hoppe, C. Linsenmann, L. Schmid, C. Willbold, and A. Wixforth, Numerical simulation of the motion of red blood cells and vesicles in microfluidic flows, *Comput. Visual. Sci.* **14**, 167 (2011).
- [79] C. Misbah, Vesicles, capsules and red blood cells under flow, *J. Phys.: Conf. Ser.* **392**, 012005 (2012).
- [80] P. M. Vlahovska, T. Podgorski, and C. Misbah, Vesicles and red blood cells in flow: From individual dynamics to rheology, *C. R. Phys.* **10**, 775 (2009).
- [81] V. Vitkova, M.-A. Mader, B. Polack, C. Misbah, and T. Podgorski, Micro-macro link in rheology of erythrocyte and vesicle suspensions, *Biophys. J.* **95**, L33 (2008).
- [82] D. Barthes-Biesel, Motion and deformation of elastic capsules and vesicles in flow, *Annu. Rev. Fluid Mech.* **48**, 25 (2016).
- [83] Z. Shen, T. M. Fischer, A. Farutin, P. M. Vlahovska, J. Harting, and C. Misbah, Blood Crystal: Emergent Order of Red Blood Cells under Wall-Confined Shear Flow, *Phys. Rev. Lett.* **120**, 268102 (2018).
- [84] B. Quaife and G. Biroso, High-volume fraction simulations of two-dimensional vesicle suspensions, *J. Comput. Phys.* **274**, 245 (2014).
- [85] A. Farutin and C. Misbah, Symmetry breaking and cross-streamline migration of three-dimensional vesicles in an axial Poiseuille flow, *Phys. Rev. E* **89**, 042709 (2014).